Dust traps and the formation of cavities in transition discs: a millimetre to sub-millimetre comparison survey

Brodie J. Norfolk,[1]★ Sarah T. Maddison,[1] Christophe Pinte [ORCID],[2,3] Nienke van der Marel,[4,5] Richard A. Booth [ORCID],[6] Logan Francis,[4,5] Jean-François Gonzalez [ORCID],[7] François Ménard,[3] Chris M. Wright,[8] Gerrit van der Plas[3] and Himanshi Garg[2]

[1]*Centre for Astrophysics and Supercomputing (CAS), Swinburne University of Technology, Hawthorn, Victoria 3122, Australia*
[2]*Monash Centre for Astrophysics (MoCA) and School of Physics and Astronomy, Monash University, Clayton, Victoria 3800, Australia*
[3]*CNRS, IPAG, Université Grenoble Alpes, F-38000 Grenoble, France*
[4]*Department of Physics and Astronomy, University of Victoria, Victoria, BC V8P 5C2, Canada*
[5]*Herzberg Astronomy and Astrophysics Programs, National Research Council of Canada, 5071 West Saanich Road, Victoria, BC V9E 2E7, Canada*
[6]*Institute of Astronomy, University of Cambridge, Madingley Road, Cambridge CB3 0HA, UK*
[7]*ENS de Lyon, CNRS, Univ Claude Bernard Lyon 1, Centre de Recherche Astrophysique de Lyon, Univ Lyon, UMR5574, F-69230, Saint-Genis-Laval, France*
[8]*School of Science, University of New South Wales, PO Box 7916, Canberra, BC 2610, Australia*

ABSTRACT
The origin of the inner dust cavities observed in transition discs remains unknown. The segregation of dust and size of the cavity is expected to vary depending on which clearing mechanism dominates grain evolution. We present the results from the Discs Down Under program, an 8.8-mm continuum Australia Telescope Compact Array (ATCA) survey targeting 15 transition discs with large ($\gtrsim$20 au) cavities and compare the resulting dust emission to Atacama Large millimetre/sub-millimetre Array (ALMA) observations. Our ATCA observations resolve the inner cavity for 8 of the 14 detected discs. We fit the visibilities and reconstruct 1D radial brightness models for 10 sources with a S/N $> 5\sigma$. We find that, for sources with a resolved cavity in both wavebands, the 8.8 mm and sub-mm brightness distributions peak at the same radius from the star. We suggest that a similar cavity size for 8.8 mm and sub-mm dust grains is due to a dust trap induced by the presence of a companion.

Key words: techniques: interferometric – planet–disc interactions – stars: pre-main sequence.

1 INTRODUCTION

Protoplanetary discs around young stars are the birth places of planets. Of particular interest are the so-called transition discs, which exhibit inner cavities in their dust distribution. They were historically believed to be the phase of transition between gaseous protoplanetary discs and debris discs, but their exact place in the evolutionary timeline (if any) still remains unknown (Espaillat et al. 2014). They were originally identified via a dip in the mid-infrared region of their spectral energy distributions (Strom et al. 1989; Wolk & Walter 1996), suggesting a deficit of micron-sized grains in the inner disc. Sub-millimetre interferometry has confirmed this deficit and resolved the inner cavity in the dust of numerous transition discs for the largest (>20 au) cavities (e.g. Brown et al. 2009; Andrews et al. 2011; Francis & van der Marel 2020).

The deficit of central emission may result from grain growth due to the vertical settling, radial drift, and coagulation of grains, resulting in a radial and vertical size sorting, and grain growth to sizes outside current observation capabilities (Tanaka, Himeno & Ida 2005). Another possible explanation is a dust trap; the trapping of dust at local maxima in the gas density (Whipple 1972;

Pinilla, Benisty & Birnstiel 2012) that can overcome the radial drift barrier (Weidenschilling 1977). Dust grains interior to this region accrete on to the host star, depleting the inner disc and forming a cavity. A number of physical mechanisms can produce dust traps in transition discs, including photoevaporation, dynamical clearing from a companion, and dead-zones (Williams & Cieza 2011; Pinilla et al. 2016).

As the accretion rate decreases, high-energy photons can impinge the accretion flow and photoevaporate the disc progressively further away. This limits the resupply of inner disc material and increases the local gas pressure at the photoevaporation front, trapping dust at the inner edge of the disc (Hollenbach et al. 1994; Clarke, Gendrin & Sotomayor 2001; Alexander, Clarke & Pringle 2006). Numerous photoevaporation models (Owen & Clarke 2012; Gorti, Hollenbach & Dullemond 2015; Ercolano & Pascucci 2017; Owen, Ercolano & Clarke 2017; Ercolano, Weber & Owen 2018) suggest that discs with an inner deficit of emission due to photoevaporative winds will have low accretion rates ($\leq 10^{-9}$ M$_\odot$yr^{-1}) and exhibit cavities with small radii ($\leq$ 10 au, see fig. 5 in Owen & Clarke 2012, or $\leq$ 20 au, see fig. 6 in Ercolano & Pascucci 2017). This is inconsistent with (sub)millimetre observations of transition discs, exhibiting cavities of tens of au in size and high accretion rates (Manara et al. 2014).

Dust traps can also result from the dynamical clearing of a companion. The formation of a planetary mass companion will

★ E-mail: brodiejamesnorfolk@gmail.com

locally deplete gas and/or dust in the disc and produce a pressure bump at the cavity edge (e.g. Paardekooper & Mellema 2004; Rice et al. 2006; Fouchet et al. 2007; Fouchet, Gonzalez & Maddison 2010; Pinilla et al. 2012), while the tidal truncation of the disc by a binary companion (e.g. Lin & Papaloizou 1979) results in a gas pressure bump at the leading edge of the truncation, consequentially trapping dust and forming a cavity as the inner disc accretes on to the host star at viscous time-scales ($\leq 10^5$ yr; Brauer et al. 2007). Dust traps formed by the presence of a companion are expected to result in a grain size distribution that mirrors the profile of the gas pressure at the maxima with larger grains strongly concentrating at the peak of the pressure profile, and smaller grain exhibiting a more extended radial structure. This is due to the relationship between the grains Stokes number and its size, as larger grains with St ~ 1 are significantly influenced by the pressure of the gas whereas smaller grains with a St < 1 are more coupled to the gas. Disc cavities have been attributed to the presence of a companion in a number of previous studies (van der Marel et al. 2016a, 2018; van der Plas et al. 2017b; Ginski et al. 2018; Pinilla et al. 2018; Price et al. 2018; Toci et al. 2020)

In regions of low ionization where the magneto-rotational instability is inhibited, there is an increase of accretion stress and subsequent local maxima in the gas pressure that can trap dust (Flock et al. 2015; Ruge et al. 2016). Models based on dust trapping at dead zone edges (Pinilla et al. 2016; Ueda, Flock & Okuzumi 2019) are highly dependent on the level of turbulence throughout the disc, and predict a similar peak in the radial distribution of sub-mm to mm dust species and strong gas depletion in the outer disc.

More than one of these physical mechanisms may occur simultaneously in transition discs. However, the dominant physical mechanism that produces a gas pressure maxima (dust trap) will result in distinct cavity sizes, accretion rates, and/or grain size distributions. As different wavebands trace dust grains of order the same size as the wavelength, multiwavelength observations of transition discs can reveal differences in the grain size distribution and further differentiate between the mechanisms behind dust trap and cavity formation.

Previous multiwavelength observations of transition discs that probe both sub-millimetre and millimetre sized grains (Casassus et al. 2015; Wright et al. 2015; Macías et al. 2018) show that each population is trapped at a similar radial position from the host star (van der Marel et al. 2015b). However, the number of sources with multiwavelength data still remains small. In this paper, we present new millimetre observations for 15 transition discs combined with archival ALMA millimetre observations, which is the largest multiwavelength survey of transition discs to date.

2 OBSERVATIONS AND DATA REDUCTION

2.1 Sample Selection

Recent high-resolution (≤ 0.2 arcsec) observations of transition discs with Atacama Large millimetre/sub-millimetre Array (ALMA) have provided a growing catalogue of discs observed at sub-mm wavelengths which show resolved dust cavities. Our Discs Down Under survey was designed to specifically complement this catalogue at 8.8 mm for Southern hemisphere sources that are observable by the Australia Telescope Compact Array (ATCA).

Our sample (see Table 1) includes 4 Herbig Ae stars (HD34282, HD100453, HD135344B, HD169142) and 11 T Tauri stars (SZ Cha, CS Cha, HP Cha, HD143006, RY Lup, J1604, J160830.7, Sz111,

SR24S, SR21, DoAr44). Three of these are located in Lupus (RY Lup, J16083070, Sz111), three in Chamaeleon (SZ Cha, CS Cha, HP Cha), and three in Ophiuchus (SR 24S, SR 21, DoAr44). One target (J1604) is a member of the Upper Scorpius Association. Three of the targets have previously been observed with ATCA in the 7-mm band at low resolution and were unresolved (Sz111 and RY Lup; Lommen et al. 2010; CS Cha; Lommen et al. 2009), and one with the VLA at 7 mm (HD169142; Dent et al. 2006).

This survey also targeted the protoplanetary disc HD163296, which is not a transition disc and hence is excluded from the analysis. Observational results for this source are presented in Appendix A.

2.2 ATCA

We used the ATCA radio telescope at 34 GHz (8.8 mm) to conduct our survey from 2016 to 2018 (project code C3119). The Compact Array Broad-band Backend (CABB; Wilson et al. 2011) provides observations with two bands that contain 2048×1 MHz channels, which we centred at 33 and 35 GHz. Observations were conducted in the 6A array configuration which has baseline lengths ranging from 337 to 5939 m and a theoretical resolution of 0.3 arcsec. The synthesized beam for each observation is detailed in Table 3. The astrometric accuracy of ATCA observations is primarily determined by the atmospheric conditions and the properties of the phase calibrators. The weather during the observations varied for each science target, and the seeing monitor RMS path-length noise for each observation is summarized in Table 2.

The science targets were observed with a sequence of 10 min on-source integration and 2 min integration of the gain/phase calibrator. The bandpass and flux calibrators were observed for $\sim$15 min and pointing checks were made on the phase calibrator every $\sim$60–90 min. All observational and calibration details are summarized in Table 2.

The data were processed using the MIRIAD package (Sault, Teuben & Wright 1995) and followed the standard procedure outlined in Section 22 of the ATCA User Guide.[1] Briefly, this involved: correcting for the frequency-dependent gain using the MIRIAD task *mfcal*; then using the flux density of the ATCA primary flux calibrator, 1937-638, to re-scale the visibilities measured by the correlator using the MIRIAD task *mfcal* with the option *nopassol* set; and correcting for the gain of the system's time variable properties due to changing conditions using the MIRIAD task *gpcal*. To reduce the noise in our data while maintaining as complete an observational track as possible, we flagged all data with a seeing monitor RMS path-length noise above 400 µm using *uvflag*, and calibrator amplitude readings that deviated more than 10 per cent from the mean flux using *blflag*. Any unusual spikes seen in the channel versus amplitude or the channel versus phase plots were also flagged using *uvflag*.

We extracted the ATCA fluxes by first concatenating the 33 and 35 GHz observations using the *uvcat* MIRIAD task, subsequently producing observations centred at 34 GHz. We then used the *fits* MIRIAD task to output the resulting uv data set as a UVFITS file and binned the visibilities using PYTHON. The total integrated fluxes were taken at zero spacing (Table 3).

After calibrating the data, images at 34 GHz were produced using robust weighting of 0.5 for uniform weighting or a *sup* value of 0 for

---

[1]https://www.atnf.csiro.au/computing/software/miriad/userguide/userhtml.html

Table 1. Discs Down Under survey source list. Distances for our sample are taken from Gaia Collaboration (2018), except for HP Cha which is taken from Whittet et al. (1997). We extract the mass accretion rates of SZ Cha from Manara et al. (2019), HD143006 from Manara et al. (2020), J1608 and Sz111 from Alcalá et al. (2017), and the remaining sources from Francis & van der Marel (2020).

Target	RA (ICRS)	Dec. (ICRS)	Distance (pc)	ATCA Observing date	ALMA ID	$\dot{M}$ (log($M_\odot$ yr^{-1}))
HD 34282	05 16 00.48	−09 48 35.4	325	10/06/2018	2015.1.00192.S, 2017.1.01578.S	< −8.30
SZ Cha	10 58 16.75	−77 17 17.2	189	03/05/2016	2013.1.00437.S	−7.65
CS Cha	11 02 24.89	−77 33 35.7	176	29/04/2016	2017.1.00969.S	−8.30
HP Cha	11 08 15.09	−77 33 53.2	160	22/05/2017	2017.1.01460.S	−8.97
HD 100453	11 33 05.58	−54 19 28.5	104	04/05/2016	2015.1.00192.S, 2017.1.01424.S	< −8.30
HD 135344B	15 15 48.45	−37 09 16.0	135	13/05/2016	2017.1.00884.S	−7.37
HD 143006	15 58 36.91	−22 57 15.2	166	04/05/2017	2016.1.00484.L	−7.79
RY Lup	15 59 28.39	−40 21 51.3	159	06/05/2016 & 06/05/2017	2017.1.00449.S	−8.20
J1604	16 04 21.66	−21 30 28.4	145	23/04/2016 & 12/05/2017	2015.1.00888.S	−10.54
J1608	16 08 30.69	−38 28 26.9	156	22/04/2016 & 13/05/2017	2012.1.00761.S	−9.1
Sz111	16 08 54.68	−39 37 43.2	158	07/05/2016 & 06/05/2017	2012.1.00761.S	−9.1
SR24S	16 26 58.50	−24 45 36.7	114	17/05/2016	2017.1.00884.S	−7.15
SR21	16 27 10.28	−24 19 12.6	138	25/04/2016	2017.1.00884.S	−7.90
DoAr44	16 31 33.46	−24 27 37.2	120	24/04/2016	2012.1.00158.S	−8.20
HD 169142	18 24 29.78	−29 46 49.3	117	15/05/2016	2016.1.00344.S	−8.70

Table 2. ATCA observing log.

| Date | Observation time (min) | Calibrators | | | Average seeing rms (μm) |
		Band-pass	Flux	Gain/Phase	
22/04/16	225	1253-055	1934-638	1606-39	380
23/04/16	225	1253-055	1934-638	1622-253	388
24/04/16	430	1253-055	1934-638	1622-253	248
25/04/16	450	1253-055	1934-638	1622-253	152
29/04/16	430	0537-441	1934-638	1057-797	202
03/05/16	340	0537-441	1934-638	1057-797	308
04/05/16	450	0537-441	1934-638	1129-58	95
06/05/16	450	0537-441	1934-638	1606-39	155
07/05/16	450	1253-055	1934-638	1606-39	170
13/05/16	450	1253-055	1934-638	1451-400	99
15/05/16	450	1253-055	1934-638	1804-251	235
17/05/16	340	1253-055	1934-638	1622-310	300
04/05/17	430	1253-055	1934-638	1622-253	185
05/05/17	450	1253-055	1934-638	1606-39	114
06/05/17	430	1253-055	1934-638	1606-39	139
12/05/17	340	1253-055	1934-638	1622-253	236
13/05/17	430	1253-055	1934-638	1606-39	196
22/05/17	320	0537-441	1934-638	1057-797	313
10/06/18	450	1921-293	1934-638	0514-161	184
12/06/18	430	1253-055	1934-638	1817-254	218

natural weighting with the *invert* task. The *sup* parameter refers to the area around the source (in arcseconds) where *invert* will attempt to suppress side-lobes. The dirty images were cleaned to 5σ (five times the RMS noise level) using the *clean* task and the beam was restored using the *restor* task. The resulting images for 13 of the 14 detected sources are presented in Fig. 1. The relatively poor seeing during the 2016 May 3 synthesis track of SZ Cha, coupled with the phase decorrelations in the visibilities, required data flagged that resulted in an unresolved image. We therefore exclude the image of SZ Cha and only present the flux determined during the period of best seeing in Table 3. Additionally, the 2018 June 10 synthesis track resulted in a non-detection of HD34282, likely a product of the low peak brightness due to its distance. As a result, we only present the 3σ upper limit in Table 3.

2.3 ALMA

The ALMA data for each source was selected from archival observations to both resolve the inner cavity of each transition disc and recover the largest spatial scales in the outer disc. The final calibrated visibilities for HD143006 were sourced from the DSHARP survey (Andrews et al. 2018). For all other discs, the highest resolution data was in ALMA bands 6 and 7 (1.3 and 0.88 mm, respectively), except for SR 24S, which has higher resolution observations in band 3 (3 mm). All ALMA data were reduced using the CASA pipeline for the appropriate ALMA cycle. Spectral lines in the ALMA data were flagged before extracting the continuum, which was time averaged to 30.5 s and a single channel per spectral window. ALMA visibilities were extracted using the *exportuvfits* in CASA and subsequently dealt with in PYTHON, with the total integrated fluxes taken at zero spacing listed in Table 3.

3 MODELLING

We quantify the relative position of the emission in the ATCA and ALMA observations using the code FRANKENSTEIN (Jennings et al. 2020) to reconstruct the 1D radial brightness profiles of the disc at each wavelength. FRANKENSTEIN is an open source code that uses a Gaussian process to reconstruct the 1D radial brightness profile of a disc non-parametrically and can in principle measure radial features smaller than the clean beam size. We use an azimuthally symmetric brightness profile model despite known asymmetries in our sample as we are solely interested in obtaining the typical cavity radius for this exercise. This is especially true for ATCA observations with elongated beams, where the poor uv-coverage effectively results in different sensitivity and bias at baselines $\geq$ 300kλ and a 1D fit of the north–south/east-west elongation. While we would ideally prefer to construct 2D models, such modelling is not feasible due to the low resolution of our ATCA observations.

FRANKENSTEIN infers the brightness at a set of N radial points given a disc outer radius (R_{max}) and assuming azimuthal symmetry. It then fits the profile to observed visibilities by using the discrete Hankel transform (Baddour & Chouinard 2015) to relate the observed visibilities to the radial brightness profile, applying a non-parametric Gaussian Process (GP) prior. The GP prior is learned from the data given two hyperparameters, α and w_{smooth}, and acts to dampen power

Table 3. Discs Down Under survey results of ATCA and ALMA continuum observations.

Target	ATCA 34 GHz flux (mJy)	ATCA 1σ rms (mJy)	ATCA θ_{beam} (as × as)	ALMA Frequency (GHz)	ALMA Flux (mJy)	ALMA 1σ rms (mJy)	ALMA θ_{beam} (as × as)	Spec. Slope (α_{mm})
HD34282	<0.290[a]	0.125	3.0 × 0.38	255	99	0.10	0.06 × 0.05	2.74
SZ Cha	0.227	0.036	0.58 × 0.32	336	294	1.65	0.21 × 0.12	3.64
CS Cha	0.483	0.062	0.43 × 0.39	341	165	0.10	0.07 × 0.04	2.29
HP Cha	0.245	0.038	0.52 × 0.34	224	59.8	0.06	0.06 × 0.04	3.08
HD 100453	0.915	0.103	0.37 × 0.27	281	209	0.36	0.06 × 0.05	2.65
HD 135344B	0.324	0.044	1.2 × 0.31	336	574	0.16	0.09 × 0.08	3.06
HD 143006	0.143	0.028	0.87 × 0.25	238	54.6	0.02	0.07 × 0.06	2.78
RY Lup	0.348	0.042	0.46 × 0.27	350	280	0.14	0.08 × 0.06	3.59
J1604	0.146	0.028	1.8 × 0.32	227	81.3	0.11	0.07 × 0.06	3.04
J1608	0.198	0.029	0.85 × 0.34	335	119	0.42	0.1 × 0.09	2.79
Sz111	0.224	0.031	0.72 × 0.36	335	160	0.41	0.1 × 0.08	2.52
SR24S	0.811	0.102	0.533 × 0.154	108	30.8	0.06	0.07 × 0.04	2.60
SR21	0.123	0.105	1.2 × 0.35	336	332	0.08	0.09 × 0.07	3.42
DoAr44	0.333	0.047	1.2 × 0.35	336	172	0.08	0.09 × 0.08	2.10
HD 169142	0.905	0.103	0.66 × 0.25	225	173	0.05	0.07 × 0.04	2.86

Note. [a]Upper limits are 3σ.

in the reconstructed brightness profile on scales where the signal-to-noise in the visibilities is low. The most pertinent parameter is α, which controls the signal-to-noise threshold below which FRANKENSTEIN does not attempt to fit the data. w_{smooth} introduces a coupling between adjacent points and prevents regions of artificially low power arising from narrow gaps in the visibilities. For more details see Jennings et al. (2020). The brightness reconstruction is not overly sensitive to variations in w_{smooth}. For our sample we set N = 250, $R_{max} \leqslant 3''$, w_{smooth} to either 0.01 or 0.0001, and vary α between 1.01 and 1.5 and then select the model with the lowest χ^2 value. However, if the data was sufficiently noisy at long baselines and the model was over-fitting, α was increased until oscillations in the fit at long baselines disappeared. We constrained our fits to be non-negative. We include Fig. B1 as an example of the fitting methodology using a variety of hyperparamaters with the resulting χ^2 values. Discs are deprojected using the inclination and position angle from high-resolution observations (see Table 4). We restrict our modelling to sources with $\sigma \geq 5$, limiting the number of sources in our sample that we model to CS Cha, HPCha, HD100453, HD135344B, RY Lup, J1608, Sz111, SR24S, DoAr44, and HD169142.

4 RESULTS

4.1 ATCA continuum emission

We detected 14 out of the 15 discs from the survey with ATCA. HD34282 was the only non-detection and we present the 3σ flux upper limit in Table 3. We spatially resolved the continuum emission of disc-like structures for 13 sources and show the CLEANed maps in Fig. 1. A deficit of emission is visible in the inner regions of HD100453, HD135344B, RY Lup, J1608, Sz111, SR24S, DoAr44, and HD169142. This can be representative of a ring-like structure in the 8.8-mm grains of these discs assuming the bulk of the emission is from thermal dust. J1604 and SR21 also appear to exhibit a deficit of central emission, but due to the low SNR for both observations this is uncertain. The structure seen in the emission of HD135344B, RY Lup, J1604, J1608, and SR24S hints at asymmetrical dust structure which is expected to become more pronounced at longer wavelengths (Birnstiel, Dullemond & Pinilla 2013; van der Marel et al. 2020). However for RY Lup, this morphology is due to the disc being

approximately edge-on (Ansdell et al. 2016; Langlois et al. 2018). The possible asymmetries in HD135344B and J1604 can not be confirmed due to the significant beam elongation, but it seems likely for HD135344B given the dust asymmetry in ALMA (van der Marel et al. 2016b). The observations of HP Cha, HD135344B, HD143006, J1604, and SR21 all suffered from a variety of poor weather conditions that required significant data flagging, resulting in sparse uv-coverage and low SNR. This makes it difficult to directly compare disc structures in the ATCA and ALMA continuum maps for these sources.

4.2 ALMA degraded continuum emission

In extended configurations of the 12-m array, ALMA has a resolutions range from 0.020 arcsec at 230 GHz to 0.043 arcsec at 110 GHz. To facilitate comparison between the ATCA and ALMA observations, we degrade the resolution of the ALMA observations to match that of the corresponding ATCA map using the *restoringbeam* option in the *tclean* task in CASA (cf. column 4 of Table 3 and column 3 of Fig. 1).

The degraded ALMA continuum maps generally present morphology similar to the ATCA continuum maps. Two symmetric intensity peaks can be seen in the degraded ALMA images that align, within reasonable radial positional accuracy, for HD100453, RY Lup, J1608, Sz111, SR21, DoAr44, and HD169142. The degraded ALMA maps for HD143006 and J1604 show morphology indicative of an inner cavity and ring-like structure. However, this is not reflected in the corresponding ATCA observations due to either the poor observing conditions or the lack of this structure in the 8.8-mm emission. For CS Cha and HP Cha, the degraded continuum maps exhibit elliptical structures similar to the corresponding ATCA observations. This suggests that any structure at 8.8 mm is not resolved by the clean reconstructed images. HD135344B exhibits two asymmetric intensity peaks indicative of its true asymmetric structure.

4.3 Visibilities and brightness profiles

4.3.1 ATCA Phase Centering

We estimate the phase centre of the ATCA observations where possible by centering the image to the apparent centre in the ring,
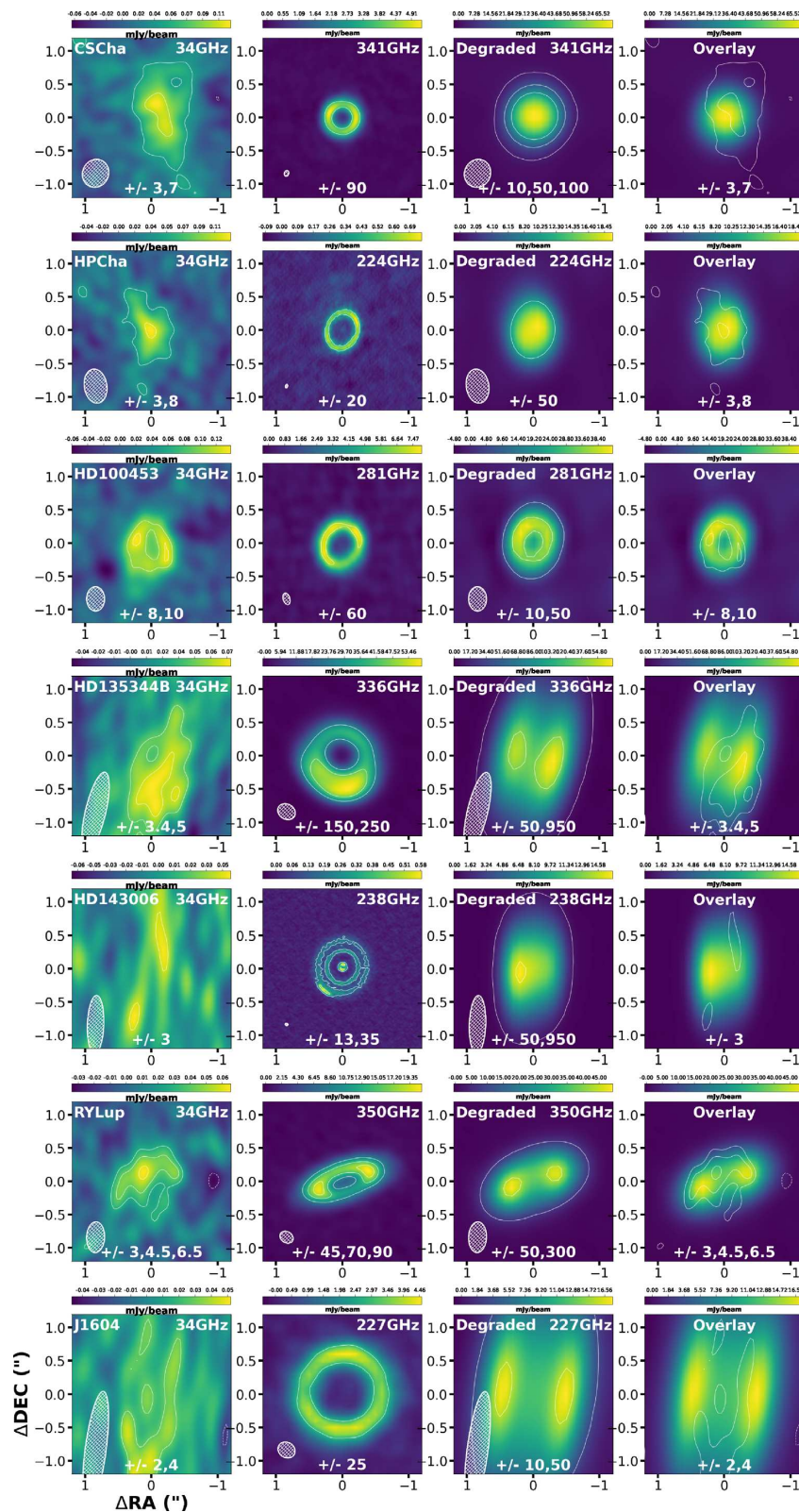
Figure 1. The 13 spatially resolved discs from the Discs Down Under survey. The 2 x 2 arcsec^2 maps show the 8.8-mm continuum ATCA maps, ALMA continuum maps, degraded ALMA continuum maps, and the ALMA continuum maps overlayed with ATCA continuum contours. The contours as printed at the bottom of each continuum map are a factor of the 1σ rms.
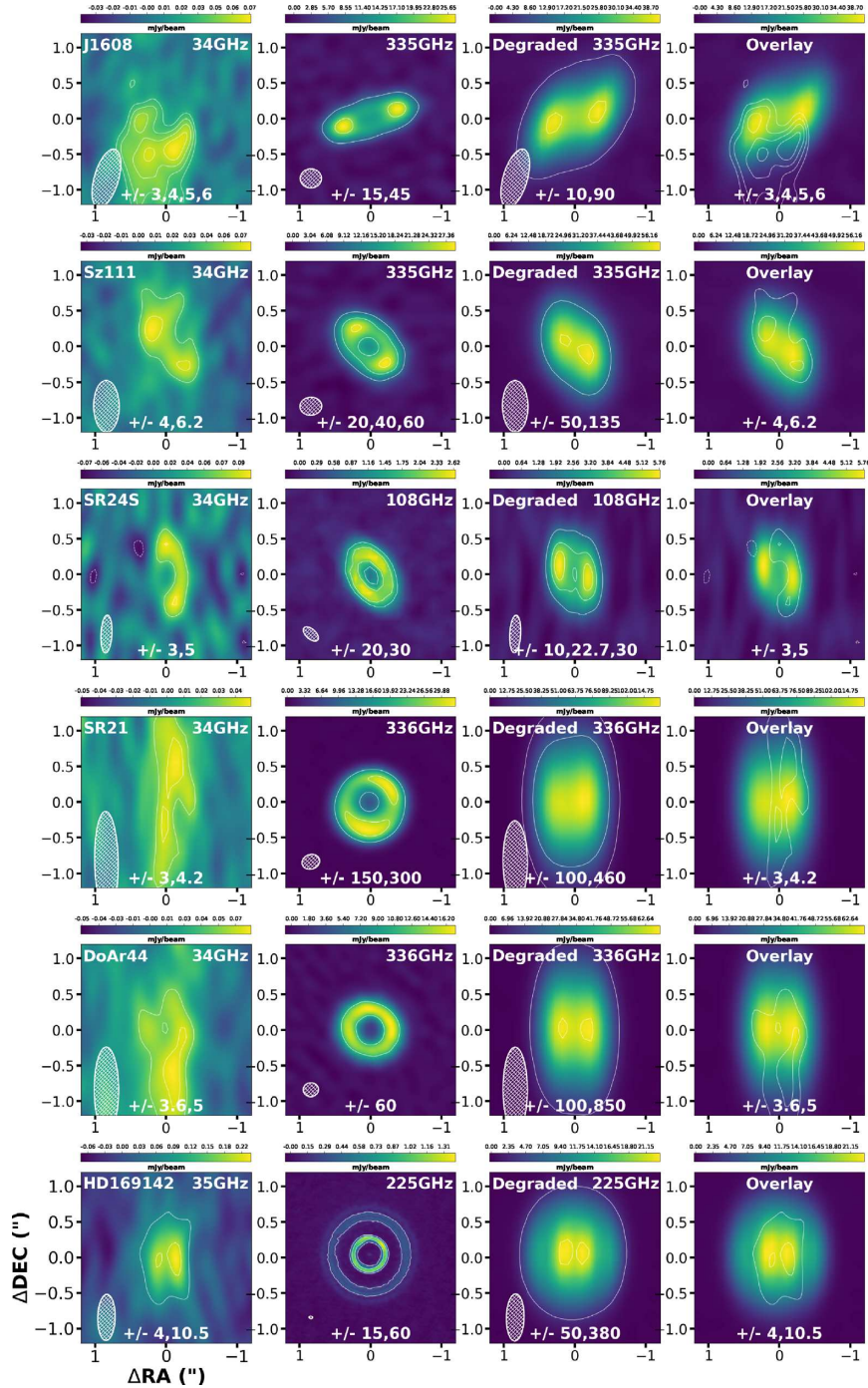
Figure 1 – *continued*

which is taken as the central deficit of emission, for about half of the sample (HD100453, HD135344B, RY Lup, J1608, Sz111, SR24S, DoAr44, and HD169142). For CS Cha, the phase centre is taken as the stellar position correct by *GAIA* proper motions. HD135344B is known to be asymmetric (van der Marel et al. 2016b), the position of central emission deficit closely corresponds to the orbital radius of the vortex derived by Cazzoletti et al. (2018; 81 au). For HP Cha this comparison could not be made as it was too faint for *GAIA* to measure its proper motion. These phase centres are consistent (∼ 0.2 arcsec) with the proper motion corrected *GAIA* positions and the accuracy is likely a function of the beam size, which can be worse in the north–

south/east–west direction for sources with extended beams (e.g. the poor north–south accuracy for DoAr44). Offsets are similar to the astrometric accuracy seen in previous ATCA observations (Wright et al. 2015).

The typical offsets of the phase centre (∼0.2 arcsec) are comparable to the cavity size of our transition discs. This directly impacts the FRANKENSTEIN 1D radial brightness models, in particular, for sources where the 8.8-mm continuum map does not resolve an inner cavity with a ring of emission but exhibits asymmetrical structure. This means that the sources that appear centrally peaked rather than ring-like (CS Cha and HP Cha) might be asymmetric as well at

Table 4. Radial brightness profile properties of the ATCA and ALMA images for sources modelled with FRANKENSTEIN. This includes the radial offset of the peak brightness R_{peak} (columns 2 and 3). We compare our FRANKENSTEIN fits with previous visibility models in column 4. Also included are the 1D profile peak positions from other models in the literature from infrared (IR) and 13CO observations, and the observed inclination and position angle of the target disc. Superscripts in the column headers refer to the position in the reference list of the last column.

Source	R_{peak} ATCA obs (arcsec)	R_{peak} ALMA obs (arcsec)	R_{peak} ALMA[a] (arcsec)	R_{peak} IR[b] (arcsec)	R_{peak} 13CO[c] (arcsec)	Incl.[d] (°)	PA[d] (°)	Reference (a,b,c,d)
CS Cha	$<0.390^a$	$0.204^{+0.007}_{-0.007}$	∓	0.102	∓	8	161	−, 8, −, 5
HP Cha	$<0.340^a$	$0.277^{+0.007}_{-0.007}$	∓	∓	∓	37	164	−, −, −, 6
HD100453	$0.307^{+0.115}_{-0.115}$	$0.306^{+0.009}_{-0.009}$	$0.24^{+0.01}_{-0.01}$	0.184	∓	29.5	151	3, 9, −, 3
HD135344B	$0.278^{+0.155}_{-0.155}$	$0.356^{+0.014}_{-0.014}$	$0.402^{+0.001}_{-0.001}$	0.363	0.292	17.7	62	1, 10, 16, 6
RY Lup	$0.412^{+0.190}_{-0.190}$	$0.436^{+0.011}_{-0.011}$	$0.452^{+0.009}_{-0.009}$	∓	0.286	68	109	1, −, 14, 7
J1608	$0.557^{+0.269}_{-0.269}$	$0.492^{+0.016}_{-0.016}$	$0.389^{+0.018}_{-0.012}$	0.288	0.300	−74	107	1, 11, 14, 8
Sz111	$0.432^{+0.189}_{-0.189}$	$0.356^{+0.015}_{-0.015}$	$0.282^{+0.020}_{-0.015}$	∓	0.225	−53	40	1, −, 14, 7
SR24S	$0.263^{+0.123}_{-0.123}$	$0.330^{+0.013}_{-0.013}$	$0.304^{+0.001}_{-0.001}$	∓	∓	46	25	4, −, −, 1
DoAr44	$0.317^{+0.163}_{-0.163}$	$0.310^{+0.014}_{-0.014}$	$0.285^{+0.001}_{-0.001}$	0.123	0.146	20	30	1, 12, 16, 1
HD169142	$0.203^{+0.089}_{-0.089}$, $0.591^{+0.099}_{-0.099}{}^b$	$0.216^{+0.010}_{-0.010}$, $0.583^{+0.017}_{-0.017}{}^b$	$0.235^{+0.034}_{-0.034}$, $0.594^{+0.034}_{-0.034}{}^b$	0.118 ∓	0.121 ∓	13	5	2, 13, 15, 2

Notes. ^{a}Upper limits are taken as the maximum cavity size (if a cavity exists) from the error for each source in Fig. 4.
^{b}Second peak.
References: (1) Pinilla et al. (2018). (2) Fedele et al. (2017). (3) van der Plas et al. (2019). (4) Pinilla et al. (2017). (5) Francis & van der Marel (2020). (6) Cazzoletti et al. (2018). (7) Ansdell et al. (2018).(8) Ginski et al. (2018). (9) Benisty et al. (2017). (10) Stolker et al. (2017). (11) Villenave et al. (2019). (12) Casassus et al. (2018). (13) Birchall et al. (2019). (14) van der Marel et al. (2018). (15) Carney et al. (2018). (16) van der Marel et al. (2016a).

8.8 mm. Fig. C1 highlights the effects on the 1D brightness models of RY Lup when moving the phase centre and cautions the interpretation of these models for sources that are possibly asymmetric (HP Cha, HD135344B, RY Lup, J1608, SR24S, and DoAr44) with relatively large beam sizes ($\gtrsim 0.2$ arcsec).

4.3.2 Multiwavelength comparison

We present the real component of the deprojected ATCA and ALMA visibilities in Fig. 2, adopting the inclination and position angle for each source from high-resolution observations (see Table 4). The imaginary components of the visibilities are presented in Fig. D1. We also present in Fig. 2 the FRANKENSTEIN reconstructed brightness profiles for the majority (10/15) of our sample and Table 4 includes the radial offsets for the peak (columns 2 and 3), R_{peak} of the FRANKENSTEIN fits. Errors in the FRANKENSTEIN fit for sources with resolved features (e.g. a Gaussian peak) are calculated via the bootstrap method. This involves fitting the disc geometry as defined by the inclination and position angle, and calculating the model numerous times using different sub-samples of the data. The bootstrap method effectively tests the 'goodness' of a fits chosen geometry and hyperparameters. As a result, if the data has a relatively high SNR and the choice of hyper-parameters is correct, sub-samples of the data will always reproduce approximately the same fit. This is apparent in our ALMA visibility fits where the 1σ error is ~ 0.4 per cent of the R_{peak} values. For further details on the bootstrap method in FRANKENSTEIN, see Jennings et al. (2020). We take the uncertainty in the R_{peak} values as the combination of the 1σ standard deviation of our bootstrap models and the full width half-maximum (FWHM) of the observational beam size. For sources with unresolved features, calculating R_{peak} and the FWHM is not possible, and the results for these sources are omitted from Table 4.

We include radial offsets from previous visibility fits in the literature and note that our values are comparable (see Table 4, column 4). The visibilities for ATCA observations that were not modelled with FRANKENSTEIN (HD34282, SZ Cha, HD143006, J1604, and SR21) and the corresponding ALMA visibilities with FRANKENSTEIN fits are included in Appendix E.

Our multiwavelength visibility comparison shown in Fig. 2 suggests that the 8.8 mm and sub-mm disc structures share a similar cavity size for HD100453, HD135344B, RY Lup, J1608, Sz111, SR24S, DoAr44, HD169142. This is indicated by the similar location of the null seen in the visibility data and similar radial positions of the Gaussian ring peak seen in the FRANKENSTEIN reconstructed 1D brightness profiles. For CS Cha and HP Cha, the 1D radial brightness profiles suggest that the 8.8 mm and sub-mm do not share a similar cavity size. For these sources, it is clear that the noise is larger than the correlated flux of the negative part in the ALMA data. It is unlikely that the FRANKENSTEIN fit for low SNR at long baselines could resolve a cavity if one is indeed present. The ATCA 1D radial brightness profiles of HD100453, HD135344B, RY Lup, J1608, Sz111, SR24S, and DoAr44 show an inner deficit of emission consistent with Fig. 1. For the ATCA data of HD169142, the FRANKENSTEIN fit is able to reproduce the two rings seen in the ALMA image that is not resolved in the ATCA image in Fig. 1, this is attributed to FRANKENSTEIN'S ability to resolve angular scales smaller than the uniform-weighted clean beam for sources with relatively low SNR at long baselines. All of the ALMA radial brightness profiles indicate a ring-like structure, as also shown in Fig. 1.

4.4 The Spectral Slope

In our multiwavelength comparison, we have assumed that the 8.8-mm emission is primarily from thermal dust, which should be tested.
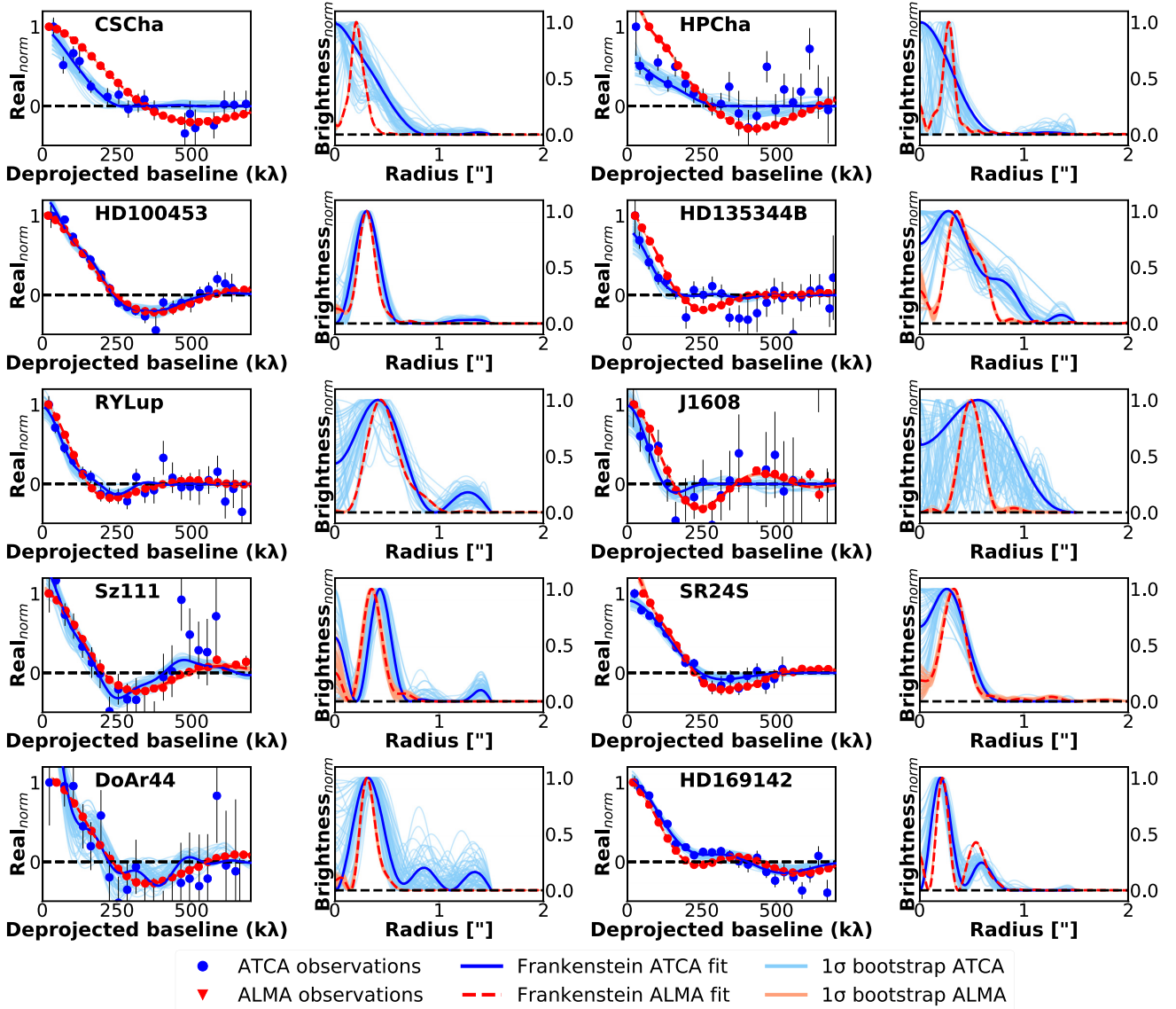
Figure 2. Normalized real component of the ATCA (blue) and ALMA (red) visibilities as a function of the deprojected baseline, and normalized FRANKENSTEIN model radial brightness profiles. The visibilities are overlaid by FRANKENSTEIN models (curves), and the model radial brightness profiles are shown with respective 1σ bootstrap error bar (see Section 4.3.2 for further details on the error calculation).

Fig. 3 shows the spectral slope between 0.8 mm and 1 cm for sources with sufficient flux measurements between 0.8 and 3.3 mm for a linear least-squares fit (in log–log space). We include a calibration uncertainty of 10 per cent for ALMA data and 20 per cent for ATCA data. Fig. 3 shows that for the majority of our sources the 8.8-mm emission falls within the fitted error, indicating that the emission is likely due to thermal dust emission from large grains. For SZ Cha and RY Lup, we see excess emission above that of thermal dust, which is likely due to free–free emission. The lack of publicly available ALMA Band 3 data for J1604 and DoAr44 result in large error bands in the spectral slope. In Table 3, we include the spectral slope (α_{mm}) calculated from our linear least-squares fit. The spectral indices for our sample range from $2.09 - 3.63$. This is consistent with a distribution of large grains (Natta & Testi 2004; Draine 2006).

5 DISCUSSION

5.1 Other sources of emission

Continuum emission at millimetre wavelengths from discs around young stars often show excess emission above that expected from a simple extrapolation of thermal dust emission observed at shorter mm wavelengths (Rodmann et al. 2006; Lommen et al. 2009; Ubach et al. 2012, 2017). This excess has been attributed to thermal free–free emission from an ionized wind, non-thermal processes such as chromospheric emission from the young stellar object, or a combination of both (Dullemond et al. 2007; Millan-Gabet et al. 2007). For thermal free–free emission, the total integrated flux can vary by a factor of $20 - 40$ per cent over a long period, while for non-thermal emission, the total integrated flux can vary by up to a factor $\gtrsim 2$ on very shorter times scales (minutes to hours; Ubach
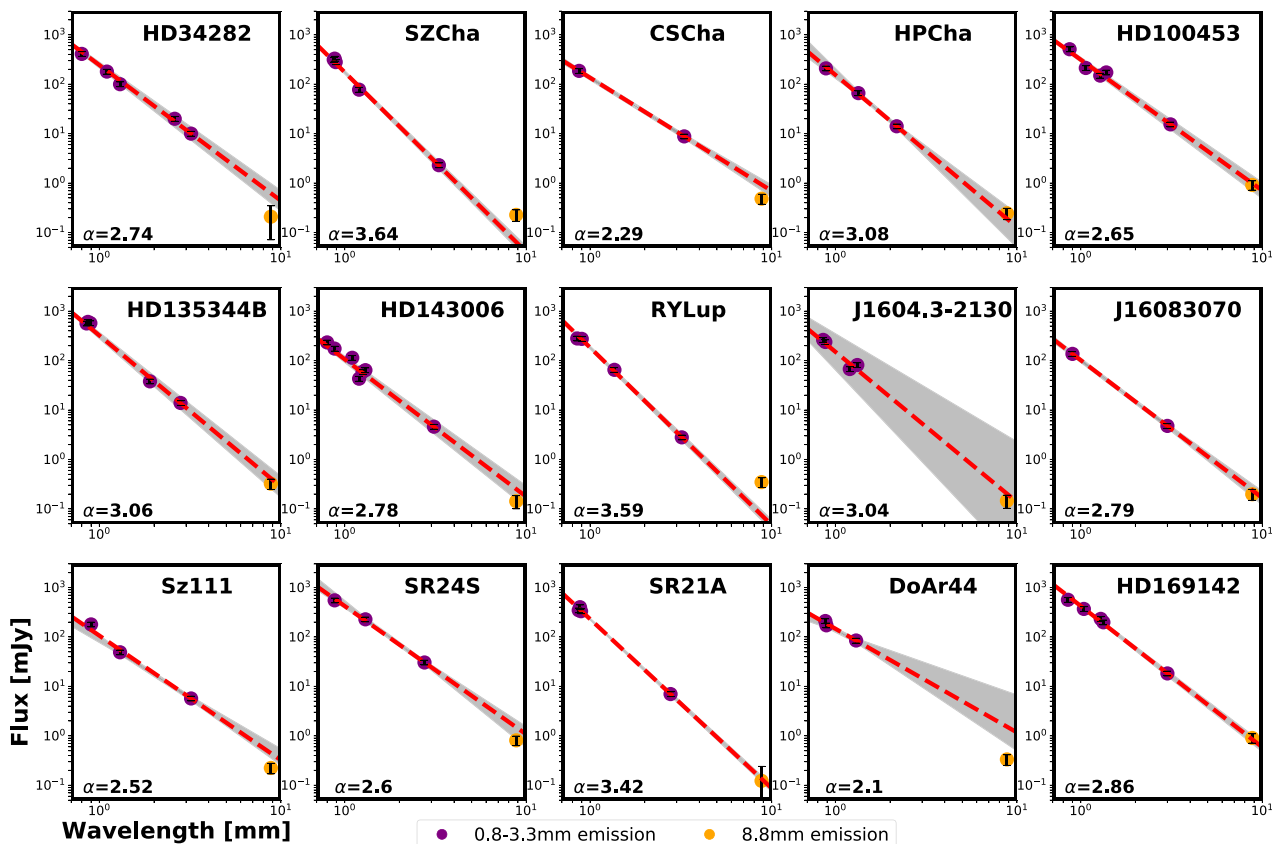
Figure 3. Spectral slopes for 14 sources in the Discs Down Under survey with observed emission between 0.8 and 3.3 mm. The error bars shown in both panels includes a calibration uncertainty of 10 per cent (ALMA) and 20 per cent (ATCA). Overplotted with grey shading are linear least-squares fits error limits to parts of the spectral slope between 0.8 and 3.3 mm.

et al. 2012). In our sample, only SZ Cha and RY Lup show an excess in emission above that expected from thermal dust. This excess is less than 40 per cent of the total integrated flux and is likely due to free–free emission. However, further observations at mm-wavelengths over a range of candences are required to confirm this. Previous temporal flux monitoring by Ubach et al. (2012) also found that RY Lup exhibits excess emission. Free–free emission has been observed in a number of other transition discs not in our sample, including HD97048 (van der Plas et al. 2017a), HD142527 (Casassus et al. 2015), and HD100546 (Wright et al. 2015). We expect the emission from the bulk of our sample to indeed be due to thermal dust, and hence the emission comparison with ALMA emission is likely a dust-to-dust comparison.

5.2 Dust traps and cavity formation

The 1D radial brightness profile models derived by FRANKENSTEIN highlight that the majority of our sample (HD100453, HD135344B, RY Lup, J1608, Sz111, SR24S, DoAr44, and HD169142) share a similar R_{peak} in both the ATCA and ALMA data. The models exhibit a Gaussian ring fit indicative of a resolved inner cavity in Fourier space that is likely due to the concentration of grains in dust traps and hence, we take R_{peak} as representative cavity size. Neither CS Cha or HP Cha share similar R_{peak} values between the ATCA and ALMA data. For these sources, the ATCA 1D radial brightness profiles suggest a disc without an inner deficit of emission and the ALMA fits suggest a ring-like morphology. As a result, if we plot R_{peak}(ALMA) versus R_{peak}(ATCA) (see Fig. 4), our sample of transition discs can be

classified into two groups: sources with similar R_{peak} values and those which only show a cavity in the ALMA data. Sources in the first group from our sample include HD100453, HD135344B, RY Lup, J1608, Sz111, SR24S, DoAr44, and HD169142. Other transitions discs in the literature which exhibit an approximately one-to-one correlation between the 8.8 mm and sub-mm R_{peak} values include HD100546 (Wright et al. 2015; Pinilla et al. 2018), GM Aur (Macías et al. 2018), LkCa15 (Isella et al. 2014; Pinilla et al. 2018), and HD142527 (Casassus et al. 2015). The second group includes CS Cha and HP Cha from our sample and HD97048 from van der Plas et al. (2017a). For the purposes of this paper, group 1 sources will be labelled resolved cavity transition discs (RC-TDs) and group 2 sources will be labelled non-detected cavity transition discs (NC-TDs).

The non-detection of cavities at 8.8 mm for the NC-TDs can reflect the lack of a cavity in the large grain population, but could also be due to large asymmetric structure resulting in either a poor model fit or inaccurate phase centering, unresolved features due to spatial resolution limitations, or the presence of other sources of emission obscuring disc features as suggested by van der Plas et al. (2017a) for HD97048. The emission for CS Cha and HP Cha appears to be dominated by thermal dust (see Fig. 3). Due to the lack of proper motions and the astrometric uncertainty of ATCA, it is possible that the emission of HP Cha is asymmetric and the chosen phase centre is incorrect (e.g. see Fig. C1), as asymmetries are expected to become more pronounced or even only revealed at longer wavelengths (Birnstiel et al. 2013; van der Marel et al. 2020). However, it is equally likely, given the low spatial resolution of the
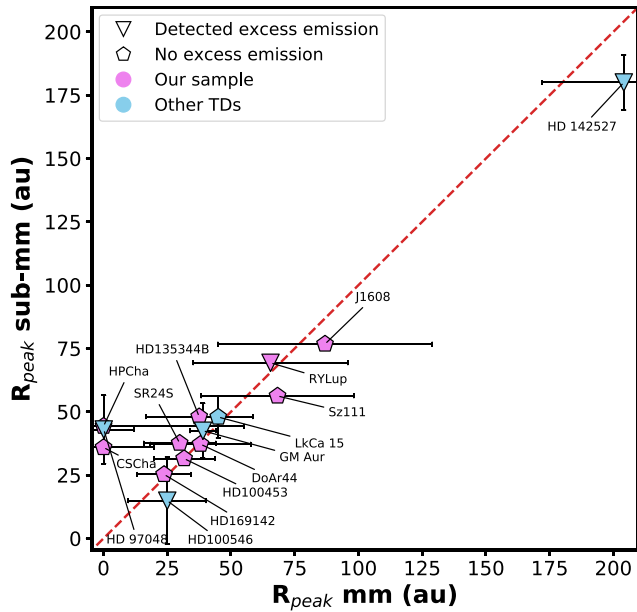
Figure 4. The $0.43 - 1.3\,\mathrm{mm}$ R_{peak} radial offsets as a function of the $7 - 9\,\mathrm{mm}$ R_{peak} radial offsets. The dashed line represents an equal radial offset at both wavelength ranges. The pentagon and triangle markers indicate whether emission other than thermal dust emission has been detected in the source as no excess or detected excess, respectively. The pink markers represent R_{peak} values from our FRANKENSTEIN modelling, and the blue markers represent R_{peak} values from the literature including: HD100546 0.86 mm data from Pinilla et al. (2018) and 7 mm data from Wright et al. (2015); GM Aur 0.9 mm and 7 mm data from Macías et al. (2018); LkCa 15 0.43 mm data from Pinilla et al. (2018) and 7 mm data from Isella et al. (2014); HD142527 1.3 mm data from Garg et al. (2020) and 7 mm data from Casassus et al. (2015); and HD97048 0.85 mm and 8.9 mm data from van der Plas et al. (2017a). The errors are a propagation of the bootstrap FRANKENSTEIN errors and the FWHM of the beam size.

ATCA observations, that a cavity exists for CS Cha and HP Cha but remains unresolved. Using FRANKENSTEIN to fit low SNR visibilities will result in poor fits not representative of the true disc features. As a result, the presence of a cavity at 8.8 mm cannot be confirmed for CS Cha and HP Cha, and more observations are required.

The exact mechanism driving large cavity formation in transition discs remains unknown (Williams & Cieza 2011). However, historically the observed deficit of inner disc emission has been attributed to either grain growth, photoevaporation, or the trapping of dust due to either dead zones or the dynamical interaction with a companion. Grain growth models (Laibe et al. 2008; Birnstiel, Andrews & Ercolano 2012b; Gonzalez et al. 2015) predict, due to the settling, growth, and inward drift of grains, that the disc will contain a size-sorted radial distribution of dust, with larger grains preferentially concentrated towards the mid-plane and host star. Previous reviews of photoevaporative models (Ercolano & Pascucci 2017) conclude that the deficit of inner emission seen in transition discs with large cavities ($\geq 20\,\mathrm{au}$) and mass accretion rates $\geq 10^{-9}\mathrm{M}_\odot\mathrm{yr}^{-1}$ cannot be attributed entirely to photoevaporation. Therefore, we suggest that neither grain growth nor photoevaporation are likely to be dominating the grain evolution in our RC-TD sources. Our sample does not show evidence of radial size sorting (Fig. 2), exhibit large cavities (Fig. 4), and the majority have modest levels of accretion (Table 1).

Magnetohydrodynamical (MHD) models of transition discs from Pinilla et al. (2016) predict a factor of 2 difference in the radial peak positions for sub-mm to mm grains at dust traps located at

the edge of dead zones (see Fig. 4 at 1 Myr in Pinilla et al. 2016) which is excluded by our one-to-one correlation seen in Fig. 4. Additionally, MHD models require a high turbulence viscosity coefficient ($\alpha \approx 10^{-2}$) in active regions of the disc (Pinilla et al. 2016; Ueda et al. 2019), which is inconsistent with observations of classical protoplanetary discs (e.g. $\alpha \approx 10^{-3} - 10^{-4}$ from Pinte et al. 2016; Flaherty et al. 2020) and previous studies of transition discs that model how inner companions influence cavity formation (Dong et al. 2017; Toci et al. 2020). Dong et al. (2017) showed with hydrodynamical simulations and radiative transfer models that the turbulence viscosity coefficient for HD169142 had to be lower than 10^{-4} for a single planet to form two distinct ring that agreed with the observations. However Toci et al. (2020), using a similar procedure but with two planets, were able to reproduce the two observed rings with $\alpha = 5 \times 10^{-3}$. Turbulence in the active regions of transition discs may not be well enough constrained to reach a firm conclusion regarding its role in cavity formation.

The dynamical interaction with a companion is proposed to be the driving force behind most features seen in transition discs including the formations of dust traps. For our RC-TDs, van der Marel et al. (2015a, 2016a, 2018) showed gas cavities inside dust cavities for SR21, HD135344B, DoAr44, J1604, Sz111, J16083070. van der Plas et al. (2019) utilized SPH and radiative transfer codes to show some disc features seen in HD100453 can be attributed to an undetected, low mass close companion within the disc's cavity. The study of HD100453 is further refined by Gonzalez et al. (2020) and Nealon et al. (2020), who show that while the outer disc morphology can be caused by a companion star on an inclined orbit exterior to the disc, the inner cavity can be explained by a $\lesssim 5\,M_J$ planet, less massive than previously suggested (van der Plas et al. 2019), at 15–20 au. Using similar 1D radial brightness profiles for the majority of our sources (HD135344B, RY Lup, J1608, Sz111, SR24S, and DoAr44), Pinilla et al. (2017, 2018) suggest that the clearing of the inner cavity could be attributed to the dynamical interaction with an embedded planet. For HD169142, Fedele et al. (2017) uses a thermo-chemical code to model the gas and dust distribution. Their results suggest that dynamical interaction between the disc and two giant embedded planets results in the depletion of the inner disc and creates two pressure bumps that aid in the trapping of dust at each observable ring position. It still remains unclear for the majority of transition discs if a companion is indeed responsible for the formation of the cavity, whether this companion is an embedded planet or a binary star. What is notable about our sample is that for the RC-TDs the 8.8 mm and sub-mm grains share a similar cavity size (R_{peak} value). This is also seen in SR24S and HD142527 (included in Fig. 4). Pinilla et al. (2019) present a planet-disc model for SR24S that predicts both mm and sub-mm grains will share a similar radial peak in the dust density. Price et al. (2018) extensively modelled HD142527 with 3D hydrodynamical simulations considering several possible orbits for the M-dwarf binary companion presented in Lacour et al. (2016). They conclude that all the observable disc features can be attributed to the tidal truncation of the disc from the binary companion. Given that our RC-TDs and HD142527 follow the one-to-one correlation shown in Fig. 4, we suggest similar physical mechanisms affecting the grain evolution for these discs may have occurred.

We include in Table 4, the IR and ^{13}CO R_{peak} values where possible for our sample. The IR and ^{13}CO R_{peak} values are consistently smaller than the corresponding ATCA/ALMA R_{peak} values, and for sources with both IR and ^{13}CO observations, the respective R_{peak} values are similar. The discrepancy between the ATCA and ALMA versus IR and ^{13}CO R_{peak} values was originally classified as the 'missing cavities' problem by Dong et al. (2012). With ATCA and ALMA

observations tracing large dust grains (sub-mm to mm sizes) and IR observations tracing small dust grains ($\sim$ μm sizes) our comparison is in agreement with dust evolution models which show large dust grains accumulate at pressure maxima (dust traps), while smaller dust grains are coupled to the gas and follow the accretion flow into the inner disc (Pinilla et al. 2012; Zhu et al. 2012; Birnstiel, Klahr & Ercolano 2012a).

6 CONCLUSIONS

In this work, we present the largest 8.8-mm continuum survey to date of transition discs with large cavities and compare the resulting dust emission to ALMA observations.

(i) For the 15 discs observed with ATCA, 14 were detected, 13 were spatially resolved, and 8 exhibited morphology indicative of ring-like structure.

(ii) The spectral slopes indicate that the emission is dominated by thermal dust for most sources, suggesting the ATCA emission is tracing the large grain population. Only SZ Cha and RY Lup showed excess emission above that from thermal dust emission.

(iii) We use the FRANKENSTEIN code to model 1D radial brightness profiles, which reveal that both the 8.8 mm ATCA and sub-mm ALMA emission in most of the discs share a similar radial position of the peak brightness, R_{peak}, suggesting a similar cavity size.

(iv) The R_{peak} values for the millimetre and sub-mm data is consistently larger than the corresponding IR and ^{13}CO R_{peak} values. This is in agreement with models indicating large grains preferentially concentrating at maxima in the gas pressure, whilst small $\sim$ μm-sized grains are coupled to the gas.

(v) We suggest that the large cavities in these transition discs result from a dust trap, likely induced by a companion.

DATA AVAILABILITY

The ATCA observational data used in this paper is available from the Australian National Telescope Facility Archive at https://atoa.atnf.cs iro.au/ under project code C3119. The ALMA observational data is available from the ALMA science archive at https://almascience.nrao .edu/aq/ under the project IDs listed in Table 1. 1D radial brightness models used the FRANKENSTEIN code which is available from https: //github.com/discsim/frank. Reduced observation data and models will be shared on reasonable request to the corresponding author.

REFERENCES

Alcalá J. M. et al., 2017, A&A, 600, A20
Alexander R. D., Clarke C. J., Pringle J. E., 2006, MNRAS, 369, 229
Andrews S. M. et al., 2018, ApJ, 869, L41
Andrews S. M., Wilner D. J., Espaillat C., Hughes A. M., Dullemond C. P., McClure M. K., Qi C., Brown J. M., 2011, ApJ, 732, 42
Ansdell M. et al., 2016, ApJ, 828, 46
Ansdell M. et al., 2018, ApJ, 859, 21
Astropy Collaboration et al., 2013, A&A, 558, A33
Baddour N., Chouinard U., 2015, J. Opt. Soc. Am. A, 32, 611
Benisty M. et al., 2017, A&A, 597, A42
Birchall E. K. et al., 2019, MNRAS, 486, 3721
Birnstiel T., Klahr H., Ercolano B., 2012a, A&A, 539, A148
Birnstiel T., Andrews S. M., Ercolano B., 2012b, A&A, 544, A79
Birnstiel T., Dullemond C. P., Pinilla P., 2013, A&A, 550, L8
Brauer F., Dullemond C. P., Johansen A., Henning T., Klahr H., Natta A., 2007, A&A, 469, 1169
Brown J. M., Blake G. A., Qi C., Dullemond C. P., Wilner D. J., Williams J. P., 2009, ApJ, 704, 496
Carney M. T. et al., 2018, A&A, 614, A106
Casassus S. et al., 2015, ApJ, 812, 126
Casassus S. et al., 2018, MNRAS, 477, 5104
Cazzoletti P. et al., 2018, A&A, 619, A161
Clarke C. J., Gendrin A., Sotomayor M., 2001, MNRAS, 328, 485
Dent W. R. F., Torrelles J. M., Osorio M., Calvet N., Anglada G., 2006, MNRAS, 365, 1283
Dong R. et al., 2012, ApJ, 750, 161
Dong R., Li S., Chiang E., Li H., 2017, ApJ, 843, 127

Draine B. T., 2006, ApJ, 636, 1114

Dullemond C. P., Hollenbach D., Kamp I., D'Alessio P., 2007, in Reipurth B., Jewitt D., Keil K., eds, Protostars and Planets V. Univ. Arizona Press, Tucson, p. 555

Ercolano B., Pascucci I., 2017, R. Soc. Open Sci., 4, 170114

Ercolano B., Weber M. L., Owen J. E., 2018, MNRAS, 473, L64

Espaillat C. et al., 2014, in Beuther H., Klessen R. S., Dullemond C. P., Henning T., eds, Protostars and Planets VI. Univ. Arizona Press, Tucson, p. 497

Fedele D. et al., 2017, A&A, 600, A72

Flaherty K. et al., 2020, ApJ, 895, 109

Flock M., Ruge J. P., Dzyurkevich N., Henning T., Klahr H., Wolf S., 2015, A&A, 574, A68

Fouchet L., Maddison S. T., Gonzalez J. F., Murray J. R., 2007, A&A, 474, 1037

Fouchet L., Gonzalez J. F., Maddison S. T., 2010, A&A, 518, A16

Francis L., van der Marel N., 2020, ApJ, 892, 111

Gaia Collaboration, 2018, VizieR Online Data Catalog, p. I/345

Garg H. et al., 2020, preprint (arXiv:2010.15310)

Ginski C. et al., 2018, A&A, 616, A79

Gonzalez J. F., Laibe G., Maddison S. T., Pinte C., Ménard F., 2015, Planet. Space Sci., 116, 48

Gonzalez J.-F. et al., 2020, MNRAS, 499, 3837

Gorti U., Hollenbach D., Dullemond C. P., 2015, ApJ, 804, 29

Hollenbach D., Johnstone D., Lizano S., Shu F., 1994, ApJ, 428, 654

Hunter J. D., 2007, Comput. Sci. Eng., 9, 90

Isella A., Chandler C. J., Carpenter J. M., Pérez L. M., Ricci L., 2014, ApJ, 788, 129

Isella A. et al., 2018, ApJ, 869, L49

Jennings J., Booth R. A., Tazzari M., Rosotti G. P., Clarke C. J., 2020, MNRAS, 495, 3209

Lacour S. et al., 2016, A&A, 590, A90

Laibe G., Gonzalez J. F., Fouchet L., Maddison S. T., 2008, A&A, 487, 265

Langlois M. et al., 2018, A&A, 614, A88

Lin D. N. C., Papaloizou J., 1979, MNRAS, 188, 191

Lommen D. J. P. et al., 2010, A&A, 515, A77

Lommen D., Maddison S. T., Wright C. M., van Dishoeck E. F., Wilner D. J., Bourke T. L., 2009, A&A, 495, 869

Macías E. et al., 2018, ApJ, 865, 37

Manara C. F., Testi L., Natta A., Rosotti G., Benisty M., Ercolano B., Ricci L., 2014, A&A, 568, A18

Manara C. F., Mordasini C., Testi L., Williams J. P., Miotello A., Lodato G., Emsenhuber A., 2019, A&A, 631, L2

Manara C. F. et al., 2020, A&A, 639, A58

McMullin J. P., Waters B., Schiebel D., Young W., Golap K., 2007, CASA Architecture and Applications, p. 127

Millan-Gabet R., Malbet F., Akeson R., Leinert C., Monnier J., Waters R., 2007, in Reipurth B., Jewitt D., Keil K., eds, Protostars and Planets V. Univ. Arizona Press, Tucson, p. 539

Natta A., Testi L., 2004, in Johnstone D., Adams F. C., Lin D. N. C., Neufeeld D. A., Ostriker E. C., eds, ASP Conf. Ser. Vol. 323, Star Formation in the Interstellar Medium: In Honor of David Hollenbach. Astron. Soc. Pac., San Francisco, p. 279

Nealon R., Cuello N., Gonzalez J.-F., van der Plas G., Pinte C., Alexander R., Ménard F., Price D. J., 2020, MNRAS, 499, 3857

Owen J. E., Clarke C. J., 2012, MNRAS, 426, L96

Owen J. E., Ercolano B., Clarke C. J., 2017, MNRAS, 472, 2955

Paardekooper S. J., Mellema G., 2004, A&A, 425, L9

Pinilla P., Benisty M., Birnstiel T., 2012, A&A, 545, A81

Pinilla P., Flock M., Ovelar M. d. J., Birnstiel T., 2016, A&A, 596, A81

Pinilla P. et al., 2017, ApJ, 839, 99

Pinilla P. et al., 2018, ApJ, 859, 32

Pinilla P., Benisty M., Cazzoletti P., Harsono D., Pérez L. M., Tazzari M., 2019, ApJ, 878, 16

Pinte C., Dent W. R. F., Ménard F., Hales A., Hill T., Cortes P., de Gregorio-Monsalvo I., 2016, ApJ, 816, 25

Price D. J. et al., 2018, MNRAS, 477, 1270

Rice W. K. M., Armitage P. J., Wood K., Lodato G., 2006, MNRAS, 373, 1619

Rodmann J., Henning T., Chandler C. J., Mundy L. G., Wilner D. J., 2006, A&A, 446, 211

Ruge J. P., Flock M., Wolf S., Dzyurkevich N., Fromang S., Henning T., Klahr H., Meheut H., 2016, A&A, 590, A17

Sault R. J., Teuben P. J., Wright M. C. H., 1995, in Shaw R. A., Payne H. E., Hayes J. J. E., eds, ASP Conf. Ser. Vol. 77, Astronomical Data Analysis Software and Systems IV. Astron. Soc. Pac., San Francisco, p. 433

Stolker T. et al., 2017, ApJ, 849, 143

Strom K. M., Strom S. E., Edwards S., Cabrit S., Skrutskie M. F., 1989, AJ, 97, 1451

Tanaka H., Himeno Y., Ida S., 2005, ApJ, 625, 414

Toci C., Lodato G., Fedele D., Testi L., Pinte C., 2020, ApJ, 888, L4

Ubach C., Maddison S. T., Wright C. M., Wilner D. J., Lommen D. J. P., Koribalski B., 2012, MNRAS, 425, 3137

Ubach C., Maddison S. T., Wright C. M., Wilner D. J., Lommen D. J. P., Koribalski B., 2017, MNRAS, 466, 4083

Ueda T., Flock M., Okuzumi S., 2019, ApJ, 871, 10

van der Marel N., van Dishoeck E. F., Bruderer S., Pérez L., Isella A., 2015a, A&A, 579, A106

van der Marel N., Pinilla P., Tobin J., van Kempen T., Andrews S., Ricci L., Birnstiel T., 2015b, ApJ, 810, L7

van der Marel N., van Dishoeck E. F., Bruderer S., Andrews S. M., Pontoppidan K. M., Herczeg G. J., van Kempen T., Miotello A., 2016a, A&A, 585, A58

van der Marel N., Cazzoletti P., Pinilla P., Garufi A., 2016b, ApJ, 832, 178

van der Marel N. et al., 2018, ApJ, 854, 177

van der Marel N. et al., 2020, AJ, 161, 27

van der Plas G. et al., 2017a, A&A, 597, A32

van der Plas G., Ménard F., Canovas H., Avenhaus H., Casassus S., Pinte C., Caceres C., Cieza L., 2017b, A&A, 607, A55

van der Plas G. et al., 2019, A&A, 624, A33

Villenave M. et al., 2019, A&A, 624, A7

Weidenschilling S. J., 1977, MNRAS, 180, 57

Whipple F. L., 1972, in Elvius A., ed., From Plasma to Planet. Wiley Interscience Division, New York, p. 211

Whittet D. C. B., Prusti T., Franco G. A. P., Gerakines P. A., Kilkenny D., Larson K. A., Wesselius P. R., 1997, A&A, 327, 1194

Williams J. P., Cieza L. A., 2011, ARA&A, 49, 67

Wilson W. E. et al., 2011, MNRAS, 416, 832

Wolk S. J., Walter F. M., 1996, AJ, 111, 2066

Wright C. M. et al., 2015, MNRAS, 453, 414

Zhu Z., Nelson R. P., Dong R., Espaillat C., Hartmann L., 2012, ApJ, 755, 6

APPENDIX A: HD163296

Here, we present the 34 GHz observations of HD163296. This source was part of the Discs Down Under survey but is not classified as a transition disc. We include the continuum 34 GHz results in Table A1 and show the continuum map in Fig. A1. The continuum map shows significant central emission likely from the combination of both the inner disc and ring structure seen in the recent DSHARP survey (Isella et al. 2018), our observations fail to resolve these features due to the lack of sufficiently long baselines and uv-coverage. No excess of emission is seen in Fig. A2.

Table A1. Integrated 7-mm flux, residual rms, synthesized beam size θ_b, and position angle for 34 GHz observations of HD163296.

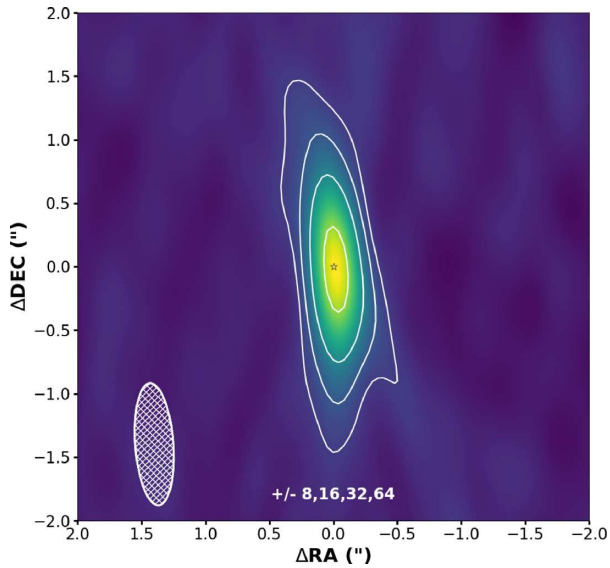| Target	ATCA 34 GHz flux (mJy)	ATCA 1σ rms (mJy)	ATCA θ_{beam} ("x")	ATCA PA$_{beam}$ (°)
HD 163296	2.45	0.0026	1.31×0.400	4.59

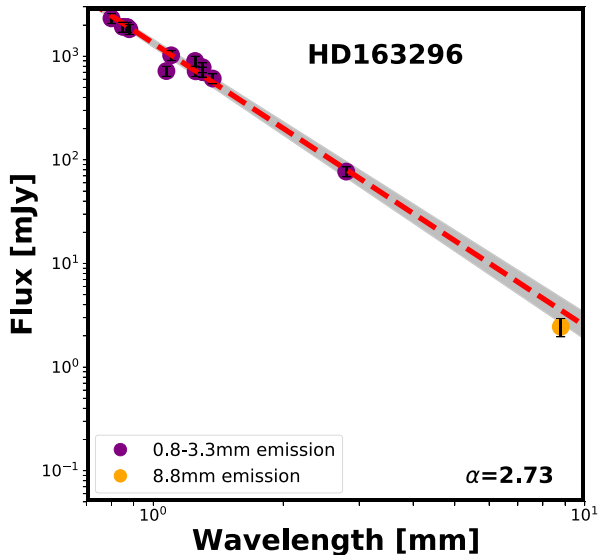**Figure A1.** 8.8-mm continuum map of HD163296.

Figure A2. The spectral slope for HD163296. Purple markers represent $0.8 - 3.3$ mm observations from ALMA and yellow markers represent 8.8-mm observations from ATCA. The error bars include a calibration uncertainty of 10 per cent (ALMA) and 20 per cent (ATCA). Overplotted with grey shading are linear least-squares fits error limits to parts of the spectral slope between 0.8 and 3.3 mm.

APPENDIX B: FRANKENSTEIN HYPER-PARAMETER SWEEP

Here, we include the FRANKENSTEIN hyper-parameter sweep for HD100453. Fig. B1 highlights the FRANKENSTEIN'S fit dependence on the selection of α and w_{smooth}. The fit is not overly sensitive to w_{smooth} which determines the length over which adjacent points are coupled. For our sample, α is varied between 1.01 and 1.5, the choice of α for each disc is determined by the characteristics of the visibility data. Values of α close to 1.01 are typically chosen for noisy data sets as FRANKENSTEIN attempts to fit longer baseline visibilities with lower SNR. As expected, Fig. B1 shows that low choices of α result in lower χ^2 values and R_{peak} values that vary minimally. However, if α is sufficiently increased the data is fit poorly (as the SNR threshold is increased) and our Gaussian ring brightness profile model may become a Gaussian centred on $r = 0$. Given the relatively large χ^2 values for these models, the difference in R_{peak} values between $r = 0$ and $r = R_{ring}$ is not a concern.
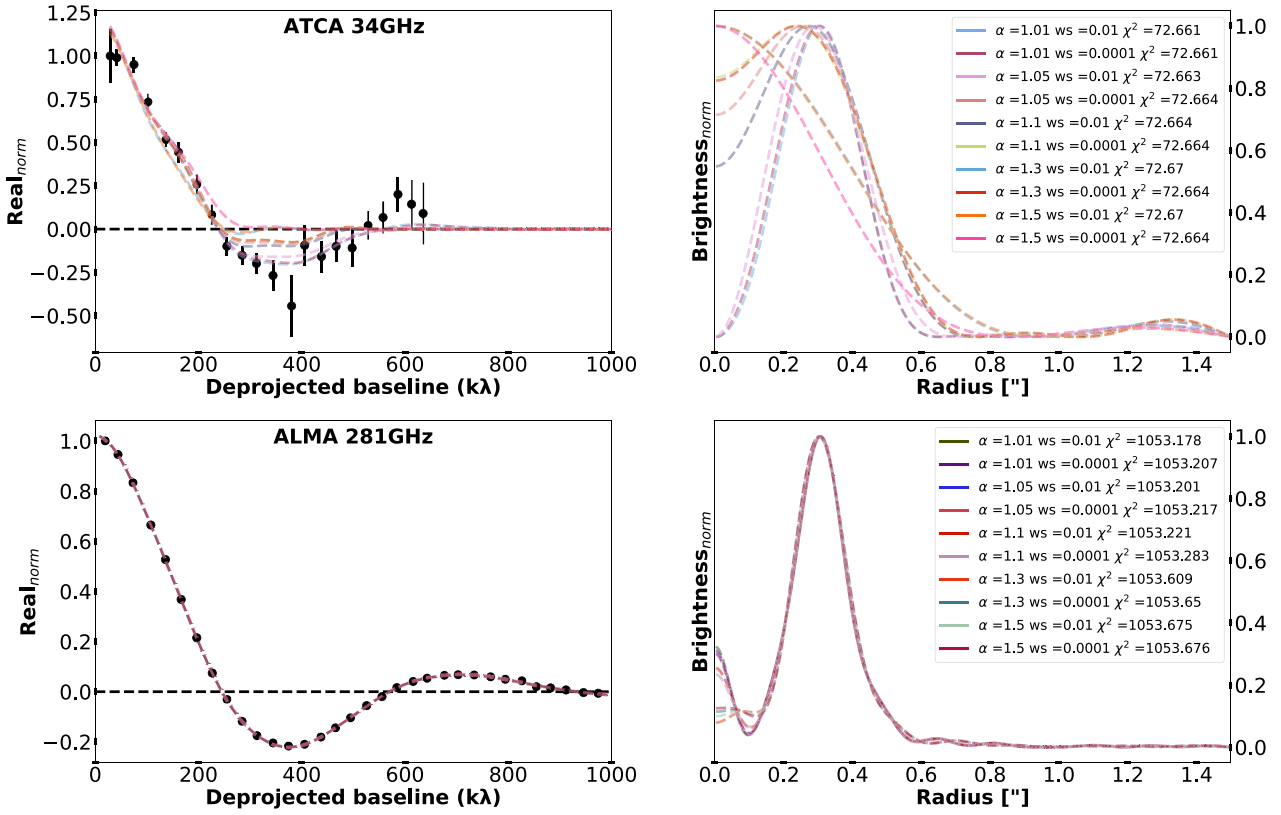
Figure B1. FRANKENSTEIN fit sensitivity to variations in both α and w_{smooth}, and the corresponding χ^2 values.

APPENDIX C: VARYING THE PHASE CENTRE

We present the visibility data and FRANKENSTEIN'S fit dependence on the phase centre. For face-on sources with an obvious deficit of central emission and a clear ring-like morphology, phase centering is simple. However, for low SNR inclined/edge-on sources finding the exact phase centre can be troublesome. Fig. C1 clearly indicates

how changing the phase centre can either produce a Gaussian-like or Gaussian ring-like 1D radial brightness profile. It is inconsequential whether we to fit this non-parametrically with FRANKENSTEIN or with a parametric model, this is an intrinsic difficulty in fitting a radial profile to a non-axisymmetric disc with uncertain phase centre. Therefore, we suggest fitting these sources should be approached with caution.
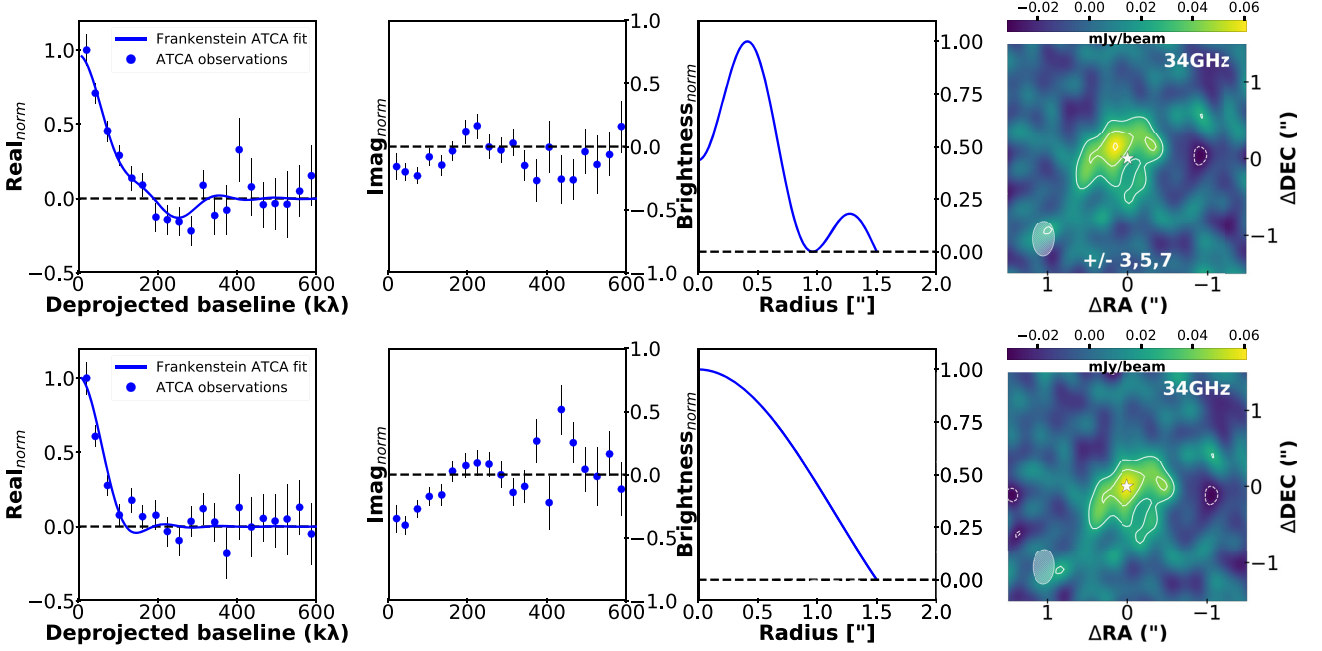
Figure C1. The effect of varying the phase centre of RY Lup on the normalized real and imaginary components of the visibilities as a function of the deprojected baseline, normalized FRANKENSTEIN model radial brightness profiles, and the 8.8-mm ATCA continuum map at two different phase centres, with offsets dRA = 0.15 arcsec and dDec = 0.4 arcsec.

APPENDIX D: IMAGINARY COMPONENT OF THE VISIBILITIES

Here, we include the normalized imaginary component of the visibilities as a function of the deprojected baseline for sources modelled with FRANKENSTEIN seen in Fig. 2. For sources with relatively high SNR in the ATCA data (HD100453, SR24S, and HD169142), the imaginary component similarly has a high SNR and a low phase instability. For the rest of our sample, the imaginary component of the ATCA indicates large phase instabilities.
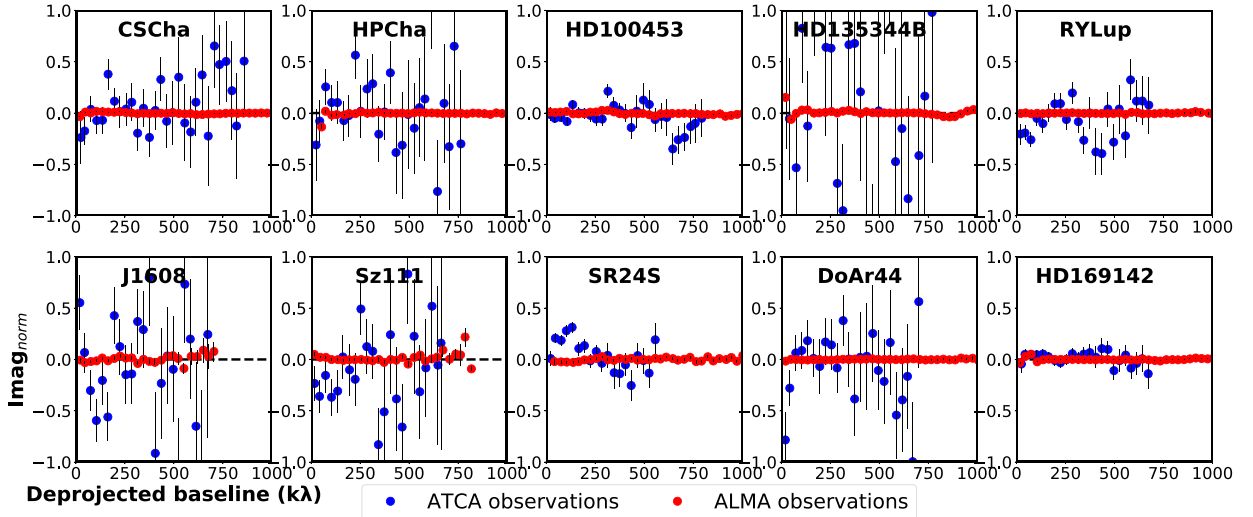
Figure D1. Normalized imaginary component of the visibilities as a function of the deprojected baseline for sources modelled with FRANKENSTEIN seen in Fig. 2.

APPENDIX E: SOURCES WITHOUT FRANKENSTEIN ATCA FITS

We include the normalized imaginary component of the visibilities as a function of the deprojected baseline for ATCA data not modelled with FRANKENSTEIN and the corresponding ALMA data with FRANKENSTEIN models. We chose not to model the ATCA data of these sources due to the low SNR ($\leq 5\sigma$) of the observations, this is obvious as shown by the large phase instability in Fig. E1. In Fig. E2, the FRANKENSTEIN fits exhibit some deviation in the reconstructed 1D radial brightness profiles. This is likely due to asymmetrical structure seen in each of the corresponding continuum maps. In our analysis, we use the same ALMA observations as Pinilla et al. (2018) for SZ Cha (Band 7), J1604 (Band 6), and SR21 (Band 7). For HD34282 and HD143006, we make use of Band 6 data and Pinilla et al. (2018) analyses Band 7 data. For HD34282, our R_{peak} value is comparable to the radial location of the peak emission presented in Pinilla et al. (2018; see table E1). However, our models

for SZ Cha, HD143006, J1604, and SR21 deviate beyond the 1σ error. The final calibrated visibilities for HD143006 was sourced from the DSHARP survey (Andrews et al. 2018) and as a result, our analysis reveals more disc substructure in comparison to Pinilla et al. (2018). For SZ Cha, J1604, and SR21, our continuum maps show a peak emission at r $\approx$ 0.430, 0.594, and 0.355 arcsec respectively, which is in close agreement with our FRANKENSTEIN fit R_{peak} values. For SZ Cha, we use robust = 0 for our briggs weighting in CLEAN and shift our visibility data to the central deficit of emission by dRA = -0.10 and dDec = -0.05. The discrepancy in the model peak brightness between this work and Pinilla et al. (2018) for these three sources is likely due to limitations introduced by adopting a singular functional form of the disc structure to fit the visibilities parametrically. These limitations are most evident in the choice of the parametric model profile which will typically poorly fit long baseline data ($\geq$ 5Mλ). The accuracy of the fit to long baseline data (on any scale) strongly influences the recovered profile's features including the radial position of the peak brightness.
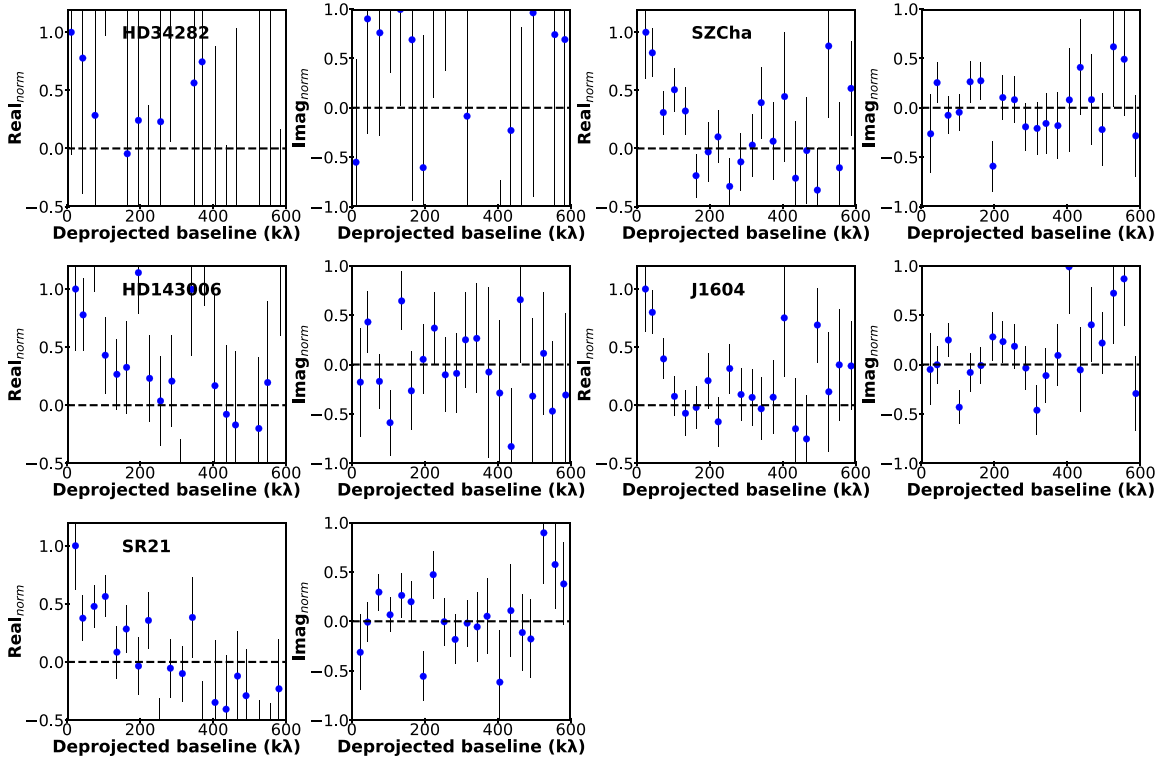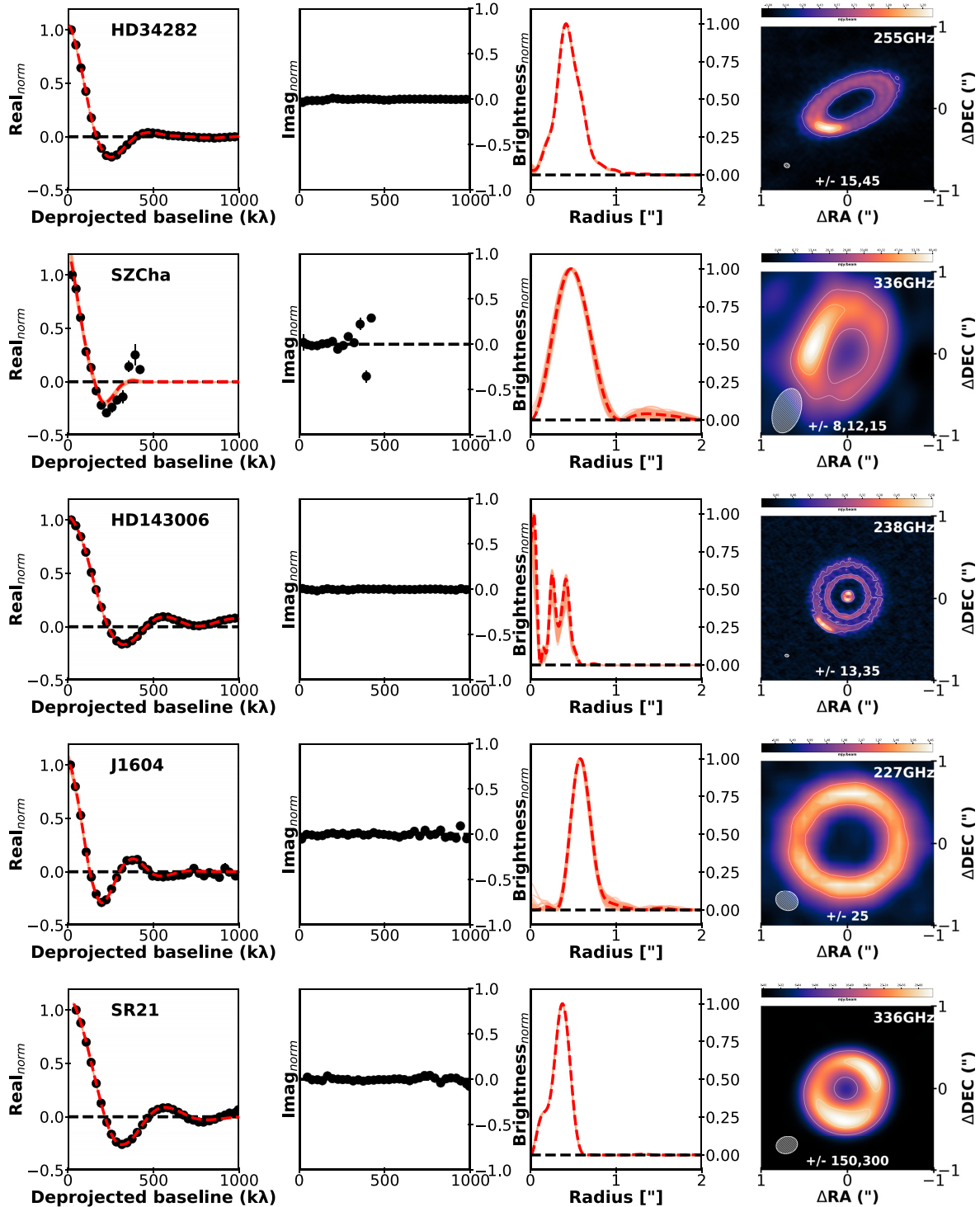
Figure E1. Normalized real and imaginary components of the visibilities as a function of the deprojected baseline for ATCA data with an SNR less than 5σ.

Figure E2. The normalized real and imaginary components of the visibilities as a function of the deprojected baseline, normalized FRANKENSTEIN model radial brightness profiles, and the sub-mm ALMA continuum map for sources not included in Fig. 2.

Table E1. Radial brightness profile properties of the ALMA for sources not included in Fig. 2. This includes the radial position of the peak brightness R_{peak}. Also included are the 1D profile peak positions from other models in the literature and the observed inclination and position angle of the target disc. Superscripts in the column headers refer to the position in the reference list of the last column.

Source	R_{peak} observations (arcsec)	R_{peak} Lit[a] (arcsec)	Incl.[b] (°)	PA[d] (°)	References (a,b)
HD34282	$0.416^{+0.001}_{-0.001}$	$0.427^{+0.001}_{-0.001}$	59	117	1,2
SZ Cha	$0.476^{+0.015}_{-0.015}$	$0.375^{+0.011}_{-0.011}$	47	154	1,1
HD143006	$0.039^{+0.014}_{-0.014}$	$0.506^{+0.006}_{-0.006}$	29.5	151	1,1
	$0.254^{+0.001a}_{-0.001}$				
	$0.413^{+0.001b}_{-0.001}$				
J1604	$0.586^{+0.007}_{-0.007}$	$0.553^{+0.010}_{-0.010}$	6	80	1,2
SR21	$0.377^{+0.003}_{-0.003}$	$0.424^{+0.001}_{-0.001}$	16	14	1,2

Notes. [a]Second Peak
[b]Third Peak
References: (1) Pinilla et al. (2018). (2) Francis & van der Marel (2020).

This paper has been typeset from a TEX/LATEX file prepared by the author.